Received: 30 June 2021 | Revised: 25 February 2022 | Accepted: 27 March 2022

DOI: 10.1002/aic.17702

RESEARCH ARTICLE

Reaction Engineering, Kinetics and Catalysis

AIChE JOURNAL

Numerical simulation analysis of the induced thrust on a char particle in reaction process

Shengyu Zhou[1,2] | Zhongjie Shen[1,2] | Qinfeng Liang[1,2] | Jianliang Xu[1,2] | Zhenghua Dai[1,2] | Haifeng Liu[1,2]

[1]Shanghai Engineering Research Center of Coal Gasification, East China University of Science and Technology, Shanghai, PR China

[2]Institute of Clean Coal Technology, East China University of Science and Technology, Shanghai, PR China

Correspondence
Jianliang Xu and Haifeng Liu, Shanghai Engineering Research Center of Coal Gasification, East China University of Science and Technology, P. O. Box 272, Shanghai 200237, PR China.
Email: xujl@ecust.edu.cn and hfliu@ecust.edu.cn

Funding information
National Natural Science Foundation of China, Grant/Award Numbers: 21878082, 21776087; Shanghai Outstanding Technology Leader, Grant/Award Number: 19XD1434800

Abstract

The force exerted on particles is of great significance to the flow and reaction characteristics of particles in gasifier. In this study, the unbalanced thrust, especially its magnitude, of a single char particle induced by chemical reactions during combustion process is investigated numerically, based on the random distribution of active sites. It is revealed that the nonuniform distribution of active sites directly leads to the nonuniform absorption of reactants and release of products, which accounts for the net induced thrust on particles. The effects of active site ratio, ambient gas temperature and particle diameter on the induced thrust of reacting particles were investigated. The results show that the induced thrust on particles could be equal to the magnitude of particle gravity. The induced thrust is determined by the nonuniformity of carbon distribution on char surface. The net thrust is enhanced with the increase of specific carbon consumption rate.

KEYWORDS
active sites distribution, chemical reaction, coal char particle, induced thrust

1 | INTRODUCTION

The efficient and clean utilization of coal is essential to reducing carbon dioxide emission. Entrained flow gasification has become an important method of coal gasification technology because of its wide adaptability of coal and high efficiency.[1] The synthesis gas from entrained flow gasifier is widely used in chemical production and polygeneration system.[2,3] In entrained-flow reactors, the char conversion is mainly in pore-diffusion controlled regime. The char conversion process plays a very important role in the operation of reactor. The movement of coal particles in the gasifier has a great influence on the heat and mass transfer of the chemical reaction.[4]

The movement of particles in entrained flow gasifier mainly considers the gravity and drag force.[5–7] The force on pulverized particles directly caused by chemical reactions is not involved at all. In previous studies, the motion phenomenon (such as particle rotation) of coal particles[8–10] was recorded in some visualization studies, like the ignition and combustion characteristics study of coal in a drop tube furnace. Recently, particle fluctuating motions[11] were recorded during combustion and gasification process of petroleum in experiments of our research group. Liu et al.[11] found that the nonuniform release of gaseous products directly accounts for particle motion. Coal particles feature the complex physical structure and the chemical composition. The irregularity of coal's shape,[12] the nonuniformity of pore distribution and material composition[13] on particles surface all lead to the movement of particles during chemical reaction process. Coal particles consist of unreactive inorganic component and reactive organic portion. The distribution of chemical substances in coal is nonuniform, as shown in Figures 2 and 3. The chemical reactivity of particles varies with the surface micro-regions. The active sites and reactivity of coal particles have been widely studied.[14–18] The pyrolysis of oxygen-containing functional groups in coal-generated active sites.[19–22] In addition, the generation of active sites during isothermal pyrolysis follows an exponential compound function with pyrolysis time.[19,21] The number of active centers is related to the internal surface area and porosity of particles.[23] Breakdown of C—H contributes to the

formation of C active sites.[24] The active sites usually exist at the crystallite edges of macropores and mesopores of char. The crystallite edges have the defects of carbon crystallite or catalytic minerals.[24,25] For individual particle, the distribution of active sites on surface is random. The reactivity varies with different micro areas.

The simulation studies of a reacting single coal particle usually focus on the conversion characteristics and the reaction dynamics. Richter[26] and Nikrityuk[27,28] respectively studied carbon consumption rates and influence of heterogeneous kinetics under different conditions through the steady-state simulation of char particle surface. They assumed that the coal particle was ash-free nonporous carbon. Sadhukhan[29,30] analyzed the dynamics of nonporous coal char by shrinking sphere model and shrinking core model. Random pore model is often used to consider the influence of pore structure in the evolution of coal char. Sadhukhan[31] studied the combustion characteristics of porous coal char particles by the volume reaction model. Beckmann[32] studied the oxidation process of coal char and measured the kinetic parameters for heterogeneous reactions. Dierich[33] and Nguyen[34] respectively explored the influence of particle velocity on the dynamics of particle porosity and the morphology evolution of porous char particles. Xue[35,36] and Richter[37] established real pore structures in the physical model. All the researches of coal char particles focus on the consumption characteristics and morphology evolution of particles. The study of chemical reaction on particle dynamics is vacant.

The particles randomly moved[11] and rotated[38] during the gasification/combustion process. These studies on pulverized coal motion during chemical reactions were only focused on experimental phenomena. The force on reacting micro-area is contributed by gaseous reactants and products fluxes according to momentum conversion, as shown in Figure 1. Coal char is an irregular porous particle with complex composition. The nonuniform gas–solid phase reactions caused a net force and torque on irregular particles. The magnitude of net force and its influencing factors are still unknown and worth further investigation. The numerical investigation for the force magnitude on nonporous particle induced by nonuniform gas–solid phase reactions (first proposed by Liu et al.[11]) is carried out in our work to further reveal the movement characteristics of reacting particles. This net force is defined as induced thrust in this paper.

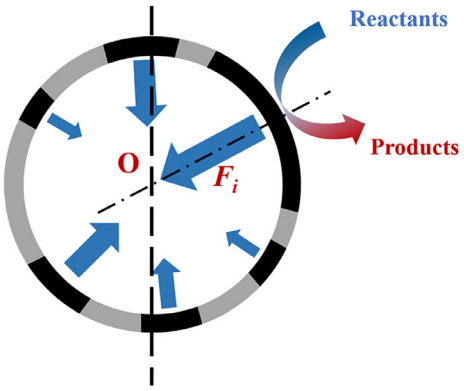

FIGURE 1 Schematic of the nonuniform reactivity on particle surface and the formation of force on active micro-area during gas–solid phase reaction process, ash (gray), carbon (black). The nonuniform reactivity directly leads to the formation of a net force on particle

In this work, the force magnitude is investigated numerically for the difficulty of experimental measurement. The random distribution model of active sites on the surface is innovatively provided to explore the effect of chemical reactions on particle dynamics. A comprehensive model including inward and outward heat transfer of reacting particles is developed to calculate the induced thrust of combustion char particle. The magnitude of induced thrust produced by chemical reactions is quantitatively studied by numerical simulation method. The effects of active site ratio, ambient gas temperature, and particle diameter on the induced thrust of reaction particle are investigated.

2 | PHYSICAL AND MATHEMATICAL MODELS

2.1 | Formation of induced thrust

The petroleum coke particles have fluctuating motions during combustion and gasification process.[11] The nonuniform gas–solid phase reactions directly account for the unbalanced force on particles. The surface reactions mainly occur at the active sites.[22] As illustrated in Figure 1, the reactive-area bears a momentum from gaseous reactants and products during the gas–solid reaction process. The thrust F_i is perpendicular to the reactive area and point to the centroid O for spherical particles. The net force on the whole particle results from the nonuniform reactivity of particle surface. The thrust F_i on reacting surface is contributed by the reaction reactants and products fluxes according to the momentum conversion.

$$\vec{F}dt = d\left(m\vec{v}\right) = md\vec{v} + \vec{v}dm, \tag{1}$$

$$\vec{v} = \frac{1}{\rho A_s \vec{n}_s}\frac{dm}{dt}. \tag{2}$$

The first term, $md\vec{v}$, on the right-hand of Equation (1) is second order. Thus, Equation (1) is expressed as

$$\vec{F} = \vec{v}\frac{dm}{dt}. \tag{3}$$

The dm/dt (kg/s) is the reaction rate, which is obtained by the numerical simulation. The gaseous reactants/products to/from particle surface are also calculated. Based on Equation (3), the pressure on reacting surface is defined as

$$p_s = v_r\frac{dm_r'}{dt} + v_p\frac{dm_p'}{dt}, \tag{4}$$

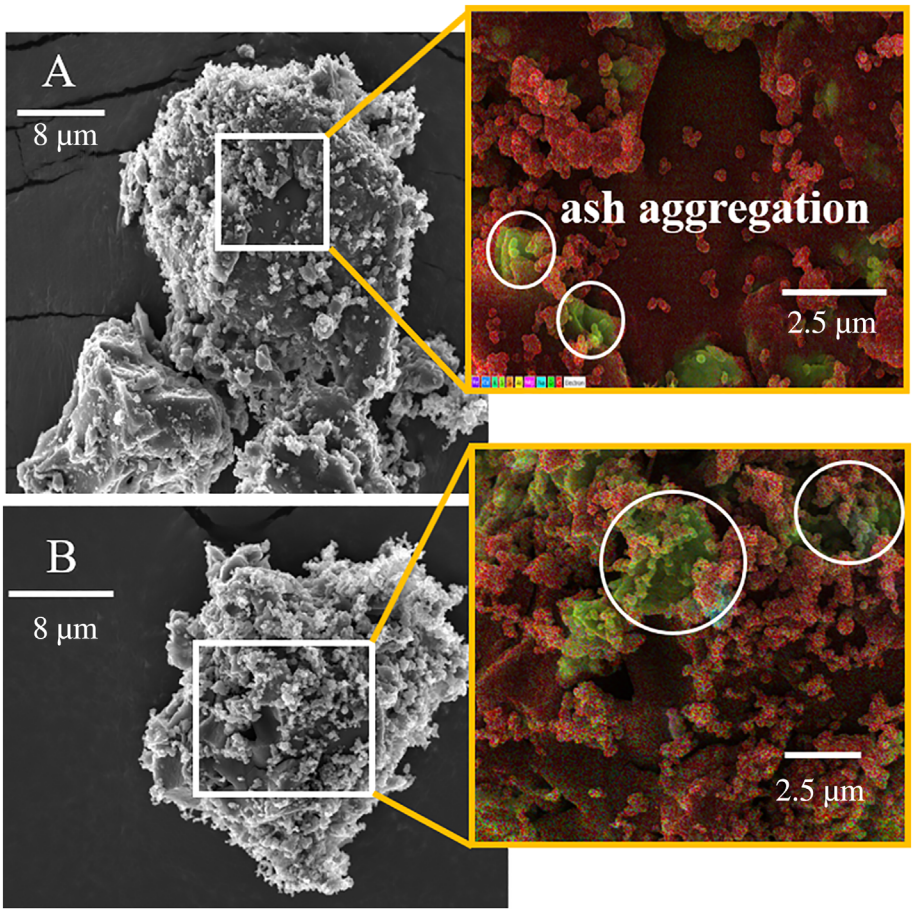

FIGURE 2 Micrographs of two char samples (A) and (B) by field emission scanning electron microscopy (FESEM) and carbon/ash analyses on particle surface, carbon (red), ash (other). (The distribution of ash aggregations is nonuniform)

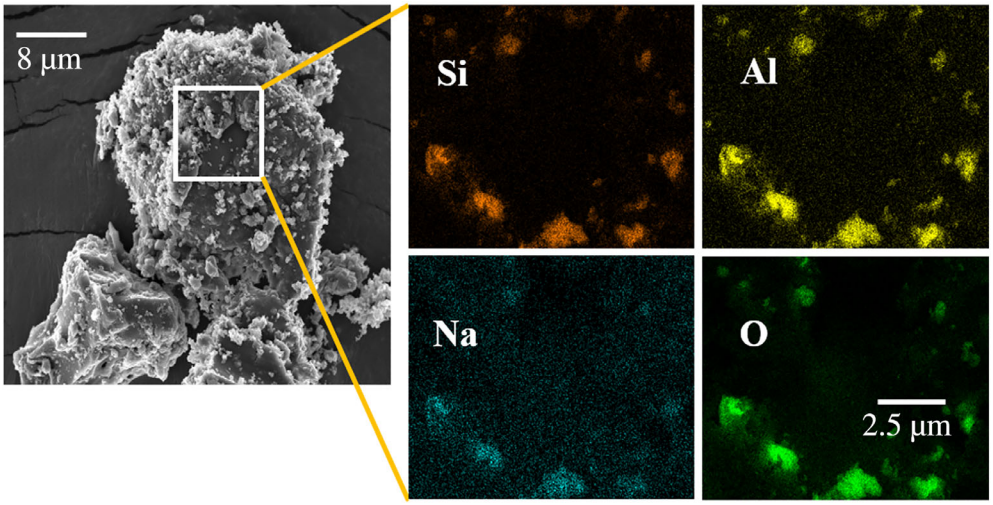

FIGURE 3 Main elements of ash distribution on micro-area of char sample A, Si (orange), Al (yellow), Na (blue), O (green). (Ash is composed of different minerals)

here, dm'_r/dt (kg/m^2/s) is the absorption rate of gaseous reactants, dm'_p/dt(kg/m^2/s) is the release rate of gaseous products. The net force induced by gas–solid phase reactions is defined as induced thrust in this article. The induced thrust $\vec{F}$ is obtained by integrating pressure at particle surface and can be expressed as:

$$\vec{F} = \sum_{i=1}^{n} p_s A_s \vec{n}_s, \tag{5}$$

where p_s is the pressure on reacting surface, A_s is area of reacting surface, $\vec{n}_s$ is the normal unit vector of reacting surface. In order to study the magnitude of induced thrust more intuitively, this thrust is compared with the particle gravity in this article. $\mathcal{F}$ is defined as the ratio between the induced thrust magnitude and the particle gravity.

$$\mathcal{F} = \left|\vec{F}\right| / m_s g. \tag{6}$$

2.2 | Active sites modeling

The nonuniformity of particle reactivity is a necessary condition for the generation of induced thrust, as shown in Figure 1. In general modeling of coal char particles, the particles are assumed to be isotropic spheres. The elements composition of char particle is complex. In order to study the distribution characteristics of reactive micro-area on the char particle surface, the morphologies and structures of Zhongmeng (ZM) bituminous coal char (composition as shown in Table 1) were measured by field emission scanning electron microscopy (FESEM), as shown in Figure 2. With the FESEM, the qualitative elements analysis on different micro areas of particle surface was obtained. Si, Al, and Na are the main inorganic components of ash on the char surface as shown in Figure 3. Ash is locally enriched on the particle surface. The ash aggregation is randomly distributed on the surface, and its characteristic size is 2–6 μm. The random distribution of ash aggregations leads to the nonuniform distribution of reactive micro-area on the particle surface.

Based on the characteristic size and the random distribution of ash aggregations shown in Figures 2 and 3, the active sites distribution model is proposed. For calculation feasibility and study simplification, several assumptions for the active site distribution model are introduced as follows. (1) The char particle consists of carbon and ash because the proximate analysis of coal char (as shown in Table 1) shows that volatile matter is merely about 2%. The volatile matter of particles is not considered. The pore structure development is a typical characteristic during char conversion process. Sadhukhan[13] studied the porous structure characteristics of coal char and proposed a modified random pore model to define the active surface area. Considering the complexity of particle evolution process, the porosity of the particle is not taken into account, thus the interparticle diffusion is neglected. Chemical reactions only occur at active sites (carbon) on particle surface. (2) The char particle surface is divided into many cells, as shown in Figure 4A. Each cell is a potential reaction site, which can be set as active or inactive site. (3) Each cell has the same probability to be an active site. The probability is equal to the ratio of active surface area and particle total surface area. The proximate analysis of coal char (as shown in Table 1) shows that fixed carbon accounts for about 70% of the total weight. The active area ratio 0.7 is estimated by the ratio of fixed carbon for this coal char. Figure 4A shows the active sites distribution for active area ratio 0.7. It should be noted that for the same active area ratio, there are many kinds of active sites distributions on particle surface. Figure 4A is only one of random distributions of active sites. The induced force on particle discussed in our work is a statistical average value for different active sites distributions at the certain active area ratio. Detailed instruction of statistical average value is shown in Section 4.1. The active area decreases with the consumption of carbon during reaction proceeding. At the same time, the active area ratio varies with different coal char. In our work, the ratio of active sites is varied in the range of 0.1–1 to systematically investigate the influence of active sites. Thus, the real active area ratio in the process of evolution is within the scope of this study. Figure 4B1,B2 shows active site distributions for $a = 0.7$ and 0.5 respectively to visually show the distribution difference for different active site ratios. Although the probability of reactivity is the same for each cell, for a single particle, the distribution of active sites on the particle surface is not absolutely uniform. Thus, the particle bears a net force as illustrated in Figure 1.

2.3 | Mathematical modeling

The chemical reaction process on the char particle surface is very complex, including the distribution of combustible materials, the diffusion of chemical reactants, heat transfer, and species conservation. The reaction model, heat-transfer model, and the flow model near particles are established based on the active site distribution model.

TABLE 1 Proximate and ultimate analysis of the char sample

Proximate analysis (wt.%, air-dried basis)				Ultimate analysis (wt.%, air-dried basis)			
Moisture	Volatile matter	Ash	Fix carbon	Carbon	Hydrogen	Nitrogen	Sulfur
0.94	2.11	26.76	70.19	63.88	0.40	0.72	0.92

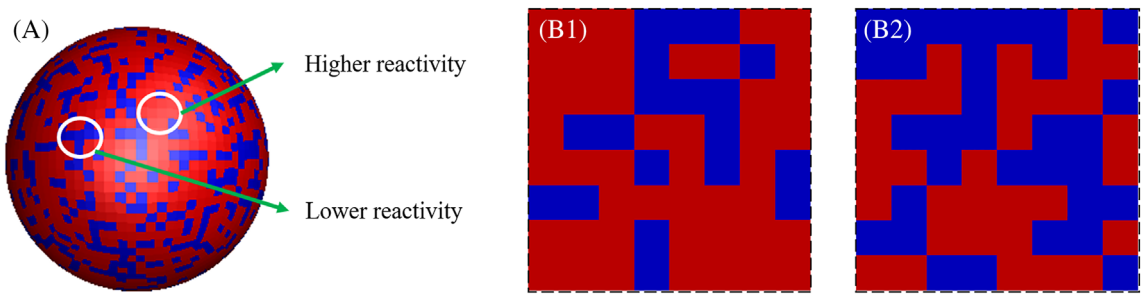

FIGURE 4 (A) Active sites distribution on particle surface, active sites (red), nonactive sites (blue). (B) Partial schematic of active sites distribution on particle surface for different active surface area ratio. (B1) 0.7-higher active surface area ratio; (B2) 0.5-lower active surface area ratio

2.3.1 | Chemical reactions

The chemistry is modeled by semiglobal reactions, with three homogeneous and four heterogeneous reactions, written as follows:

$$CO + 0.5O_2 + H_2O \rightarrow CO_2 + H_2O, \quad (R1)$$

$$CO + H_2O \rightarrow CO_2 + H_2, \quad (R2)$$

$$CO_2 + H_2 \rightarrow CO + H_2O, \quad (R3)$$

$$C + CO_2 \rightarrow 2CO, \quad (R4)$$

$$C + 0.5O_2 \rightarrow CO, \quad (R5)$$

$$C + H_2O \rightarrow CO + H_2, \quad (R6)$$

$$C + O_2 \rightarrow CO_2. \quad (R7)$$

The semi-global reaction rates of three homogeneous[26,39,40] and four heterogeneous[41–43] chemical reactions are showed in Tables 2 and 3. The catalytic effect of water vapor on CO combustion was considered.[39] The forward and backward water-gas shift reactions were selected.[28,37] The rate constant for reaction r follows the Arrhenius expression:

$$k_r = A_r T^{\beta_r} e^{-E_a/RT}, \quad (7)$$

here, A_r is pre-exponential factor, β_r is temperature exponent, and E_a is activation energy for the reaction.

2.3.2 | Particle inward heat-transfer model

In this article, the steady-state approach is applied for char burning. The internal entity of particle is neglected.[26–28,37] The surface exothermic reactions of particles generate a lot of heat, including inward and outward heat transfer. The chemical reactions produce heat Q. Q_1 is the heat transfer to particle interior from particle surface. Q_2 is the heat transfer to the gas in flow field. The heat flux Q_1' of inward heat transfer is calculated as follows:

$$Q = Q_1 + Q_2, \quad (8)$$

$$Q_1 = m_s c_p \Delta T, \quad (9)$$

$$\Delta T = T_s - T_\infty, \quad (10)$$

$$Q_1' = \frac{Q_1}{S \cdot \tau_t} = \frac{4/3\pi {r_s}^3 \rho_s c_p (T_s - T_\infty)}{4\pi r^2 \tau_t} = \frac{r_s \rho_s c_p (T_s - T_\infty)}{3\tau_t}, \quad (11)$$

where m_s is the particle mass, r_s is the particle radius, c_p is the specific heat capacity, ρ_s is the coal char density, 1400 kg/m^3. T_s and T_∞ are the surface temperature of particle and the ambient temperature, S is the particle surface area. τ_t is the heat transfer time, which can be modeled as following formula:

$$\tau_t = \eta \cdot \tau_b, \quad (12)$$

where τ_b and η are the char particle burning time and the proportional of heat transfer time during the particle combustion process. According to the work of Riaza,[8] the rapid heating time of coal particles accounts for 0.09–0.12 of the burnout time. So, the coefficient η is given as 0.105. For the τ_b, it is mainly affected by particle size, temperature, and gas composition in the flow field. The diffusion-controlled combustion of char particle follows the d^2-law,[44] which can be expressed as:

$${d_0}^2 - d^2(t) = k_c t, \quad (13)$$

$$k_c = \frac{4\rho \mathrm{Nu_D}^* D}{\rho_c} \ln(1 + B), \quad (14)$$

$$B = \frac{2w_{O_2,\infty} - \frac{v_s - 1}{v_s} w_{CO_2,s}}{v_s - 1 + \frac{v_s - 1}{v_s} w_{CO_2,s}}, \quad (15)$$

where $v_s = 44/12 = 3.664$, ρ is the gas density, ρ_c is the carbon density, D is the gas mass diffusion coefficient,[45] $w_{O_2,\infty}$ and $w_{CO_2,s}$ are the mass fraction of O_2 and CO_2. $\mathrm{Nu_D}^*$ equals 2, when the char particle is pure diffusion-controlled combustion without the influence of convection. The burnout times calculated by Equations (13)–(15) for different diameters are compared with Makino's[46] values, when the

TABLE 3 Reactions rates for heterogeneous reactions

Reaction	A_r	E_a (J/kmol)	β_r	Ref
R4	4.605 m/(s/K)	1.751×10^8	1	41
R5	3.007×10^5 m/s	1.4937×10^8	0	42
R6	11.25 m/(s/K)	1.751×10^8	1	41
R7	593.83 m/(s/K)	1.4965×10^8	1	43

TABLE 2 Reaction rates for homogeneous reactions

Reaction	R_i (kmol/m^3/s)	A_r	E_a (J/kmol)	β_r	Ref
R1	$K_{CO}[CO][H_2O]^{0.5}[O_2]^{0.25}$	2.24×10^{12}	1.6736×10^8	0	39
R2	$K^f[CO][H_2O]$	2.74×10^9	8.368×10^7	0	40
R3	$K^b[CO_2][H_2]$	9.98×10^{10}	1.205×10^8	0	26

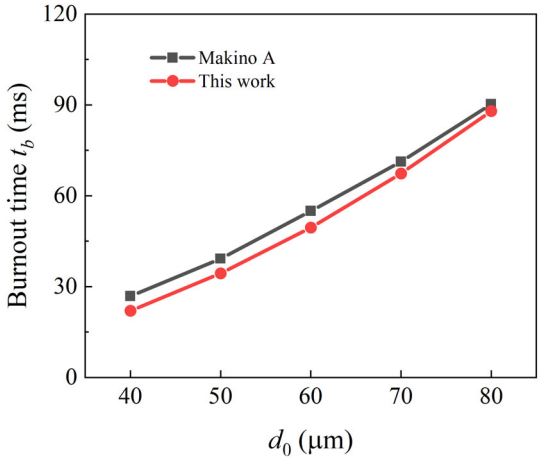

FIGURE 5 Burnout time for different diameters

ambient temperature is 1400 K and the mass fraction of O_2 is 0.4. The average deviation is 9.6%, as shown in Figure 5. The estimation of burnout time is valid. The heat flux Q_1' of inward heat transfer is considered on the particle surface according to Equation (11).

2.3.3 | Flow field and heat-transfer process

In this work, the Pseudo-steady-state approach is adopted, because the consumption time scale of the particle is always long compared to the diffusion and convective time of the gas phase.[39] The buoyancy effect on the particle is ignored. The Navier–Stokes equations coupled with the energy and species conservation equations are applied to solve the flow field.

Continuity and momentum equations:

$$\nabla \cdot \left(\rho \vec{v}\right) = 0, \tag{16}$$

$$\nabla \cdot \left(\rho \vec{v}\vec{v}\right) = -\nabla p + \nabla \cdot \left(\bar{\bar{\tau}}\right), \tag{17}$$

where p is the static pressure, the stress tensor $\bar{\bar{\tau}}$ is given by

$$\bar{\bar{\tau}} = \mu\left[\left(\nabla \vec{v} + \nabla \vec{v}^T\right) - \frac{2}{3}\nabla \cdot \vec{v} I\right], \tag{18}$$

here, μ is the molecular viscosity and I is the unit tensor.

The mixture material is modeled by incompressible ideal gas law:

$$\rho = \frac{p}{RT\sum_i \frac{Y_i}{M_i}}, \tag{19}$$

here, R is the universal gas constant, Y_i is the mass fraction of species i, and M_i is the molecular weight of species i.

Species and energy transport equations:

$$\nabla \cdot \left(\rho \vec{v} Y_i\right) = \nabla \cdot \left(\rho D_{i,m} \nabla Y_i\right) + R_i, \tag{20}$$

where R_i is the net rate of production of species i by chemical reaction, and $D_{i,m}$ is the mass diffusion coefficient for species i in the mixture.

$$R_i = M_i \sum_{r=1}^{N_R} \hat{R}_{i,r}, \tag{21}$$

where $\hat{R}_{i,r}$ is the Arrhenius molar rate of creation or destruction of species i in reaction r.

$$\nabla \cdot \left(\rho \vec{v} h\right) = \nabla \cdot \left(\lambda \nabla T - \vec{q}_r\right) - \sum_i \frac{h_i^0}{M_i} R_i, \tag{22}$$

where λ is the thermal conductivity, h is the sensible enthalpy, h_i^0 is the enthalpy of formation of species i. The first two terms on the right-hand side of Equation (22) represent energy transfer due to conductive and radiation, and the last term is the heat of chemical reaction. For the radiation heat transfer, the $P-1$ radiation model is used,[26,37] which can be written as follows:

$$q_r = -\frac{\nabla G}{3\alpha}, \tag{23}$$

$$\nabla \cdot \left(\frac{\nabla G}{3\alpha}\right) - \alpha G + 4\alpha n^2 \sigma T^4 = 0, \tag{24}$$

$$-\nabla \cdot q_r = \alpha G - 4\alpha n^2 \sigma T^4. \tag{25}$$

Here, α is the absorption coefficient, G is the incident radiation, n is the refractive index of the medium, and σ is the Stefan-Boltzmann constant. The values for μ, λ are calculated by kinetic theory. The heat capacity of the mixture is calculated by polynomial expression.

2.3.4 | Boundary conditions on particle surface

Species diffusion effects in the energy equation due to wall surface reactions are included in the normal species diffusion term. The heat flux of particle inward heat transfer is considered by the wall boundary conditions based on Equation (11). The convective and diffusive mass fluxes of the gas-phase species at the surface are balanced by the production/destruction rates of gas-phase species caused by surface reactions.

$$\rho_{\text{wall}} D_i \frac{\partial Y_{i,\text{wall}}}{\partial n} - \dot{m}_C Y_{i,\text{wall}} = M_{w,i} \hat{R}_{i,s}, \tag{26}$$

$$\dot{m}_C = \sum_{i=1}^{N_R} M_{w,i} \hat{R}_{i,s}, \tag{27}$$

where $\widehat{R}_{i,s}$ (kmol/m^2/s) is the production rate of species i due to the surface reaction (R4–R7), $\dot{m}_C$ is the net mass flux between the surface and the gas, the index $_{wall}$ refers to the gas side at the wall.

3 | SIMULATION CONDITIONS AND METHODS

A single spherical coal char particle was placed stationarily in the center of a $266d \times 266d \times 266d$ cube flow field. The computational domain and numerical grids are presented in Figure 6. The flow field is large enough to ensure that the gaseous reactants diffuse to the particle surface. The basic numerical conditions are shown in Table 4. The ambient air is quiescent and nearly dry. Char density is 1400 kg/m^3. The char particle size used in this work varies from 60 to 210 μm. The governing equations were solved by the finite volume numerical algorithm based on the commercial software Fluent. The convection terms were discretized by means of the QUICK scheme. The SIMPLE algorithm was adopted for pressure velocity coupling. The under-relaxation factors were set as 0.8. The reaction properties of each surface cell were defined as an active site or inactive site by a random function. Then, the active and inactive sites were obtained by multiplying 1 or 0 by the reaction rate constant via user-defined functions, as illustrated in Figure 4A.

4 | RESULTS AND DISCUSSION

4.1 | Model analysis and validation

As shown in Figure 6, it is difficult to divide the spherical particle surface into regular quadrilateral with equal area. The cell area on the particle surface is slightly different. The active cell ratio and active area ratio are introduced. They are respectively defined as Equations (28) and (29).

$$a = \frac{N_r}{N_t}, \tag{28}$$

$$b = \frac{S_r}{S}, \tag{29}$$

here, N_r is the number of active cells, N_t is the total number of cells on particle surface, S_r is the active area, and S is particle surface area. In order to assess the uniformity of surface cells, the relative variance δ between a and b is defined as:

$$\delta = \frac{|b-a|}{b}, \tag{30}$$

b is calculated according to a certain a. For $a = 0.5$, the relative variance δ for different cells numbers of particle surface is shown in Figure 7A. Relative variance decreases with the increase of cells number on particle surface. The maximum deviation is less than 0.3%. Secondly, the relative variances are displayed for different active area ratios at the surface cells number of 2400, as illustrated in Figure 7B. The relative variance is less than 2% at $a = 0.01$. In the following work, the active sites proportion and distribution are represented by the ratio of the active cells number instead of the active area.

The distribution and number of active sites affect the magnitude of induced thrust on particle. The gravity in the flow field is ignored to exclude its disturbance on the induced thrust. For the same active area ratio, like $a = 0.5$, there are many kinds of active sites distributions. The distribution of active sites decides the position of

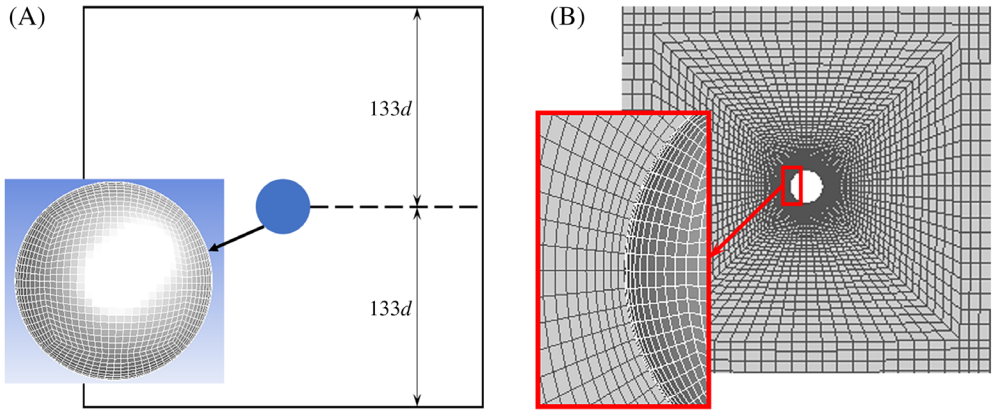

FIGURE 6 (A) Computational domain and (B) numerical grid

TABLE 4 Numerical conditions

Particle diameter d (μm)	Ambient temperature T_0 (K)	Operating pressure p (atm)	Air (mass fraction)		
			O_2	N_2	H_2O
150	1573	1	0.233	0.766	0.001

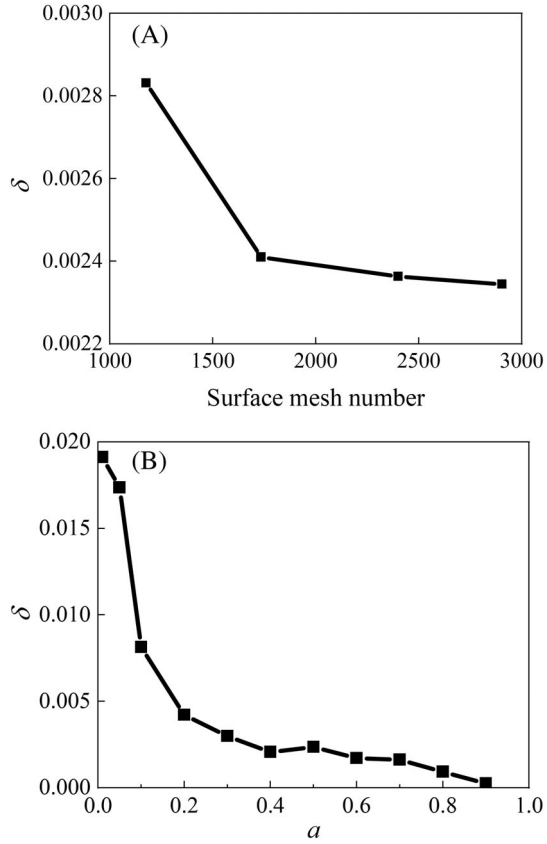

FIGURE 7 Relative variance between *a* and *b* for different (A) surface cells numbers and (B) active area ratios

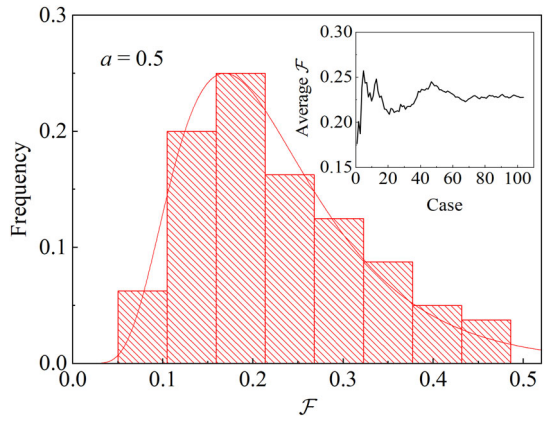

FIGURE 8 Frequency histogram of $\mathcal{F}$ ($a = 0.5$)

heterogeneous reactions. The induced thrust differs with different active sites distributions. The statistical average value of induced thrust is obtained by calculating the net forces for different active sites distributions at the same *a*. Figure 8 shows the frequency histogram of $\mathcal{F}$ for different active sites distributions at $a = 0.5$ at the surface cells number of 2400, based on the numerical conditions in Table 4. As shown in the inset figure of Figure 8, with the increase of samples, the average $\mathcal{F}$ tends to be constant. The numerical results of

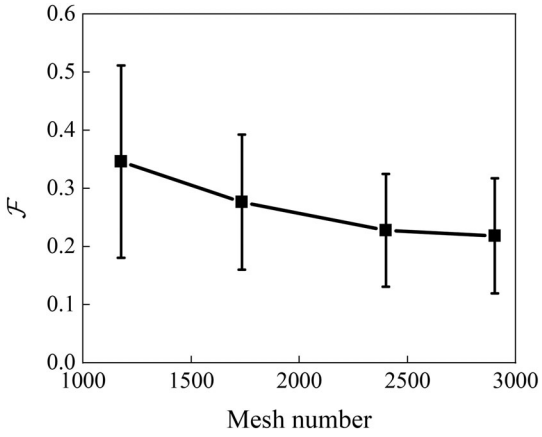

FIGURE 9 Average $\mathcal{F}$ for different mesh

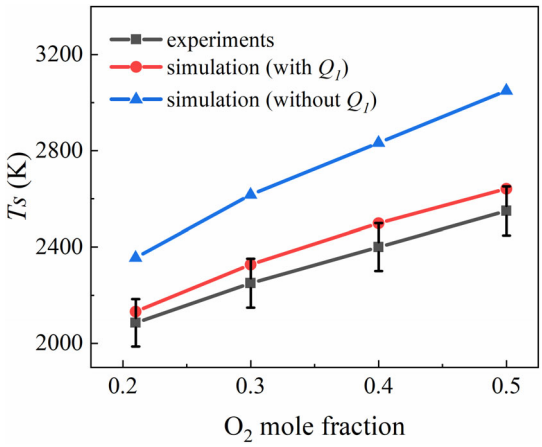

FIGURE 10 Validation against experimental data[47]

particle-induced thrust approximately follow the logarithmic normal distribution. The induced thrust discussed in our work is a statistical average value. The precision of particle surface grids has a direct influence on the induced thrust. Figure 9 illustrates the average $\mathcal{F}$ for different surface cells number. The average $\mathcal{F}$ and its standard deviation decrease with the increase of surface cells. The average $\mathcal{F}$ is basically steady when the surface cells number reaches 2400. In addition, when the particle surface grids are 2400, the size scale of the active site for the 50–200 μm particles is several microns, which is equal to the scale of ash aggregations in Figures 2 and 3. Therefore, the mesh with a surface cells number of 2400 is chosen for the following numerical study.

For the numerical simulation of thrusts induced by chemical reaction, the accuracy is affected by the surface reaction model, flow model, and heat-transfer model. In order to validate the proposed models, Figure 10 shows the comparison between our numerical results and experimental data of particle temperature published by Bejarano[47] for 90 μm particles in O_2/N_2 at 1400 K. All the simulation conditions are identical to Bejarano's experimental conditions. *Re* was estimated to be 1. Active cells number used in simulation was estimated by the ratio of fixed carbon in the experiments.[47] The

agreement is relatively good between the numerical results and experiments; the numerical results are within the experimental accuracy range. In addition, it can be found that the inward heat transfer has a great influence on the heat balance.

4.2 | Particle reaction characteristics

The heterogeneous reactions occur on the particle surface and produce gaseous products to form a net thrust. The reaction characteristics and the induced thrust of a single particle were analyzed by the numerical result of one active sites distribution at $a = 0.5$ with the numerical conditions in Table 4. Figure 11 shows the reaction rates of R4, R5, and R7. The R5 and R7 are dominant in the particle surface reactions. The reaction rate at sparsely distributed active sites is faster than that at densely distributed active sites. The consumption of gaseous reactants at densely distributed active sites is faster, and the concentration of gaseous reactants is lower. Heterogeneous reactions consume carbon and produce large reaction heat. The carbon consumption rate on particle surface and the temperature distribution around the particle are shown in Figure 12. Corresponding to the reaction rates, the carbon consumption rate at active sites aggregations is also lower. The average carbon consumption rate m' is 0.1 kg/m^2/s. The average surface temperature T_s is 2118 K.

As carbon was consumed, the gaseous products (CO and CO_2) were released outward perpendicularly at each active micro-area, forming Stefan flow on the particle surface. The gas velocity in flow field at plane $z = 0$ is shown in Figure 13. The velocity distributions in x and y directions are also depicted. The gas velocity decays gradually, tending to 0 at about $x = 4d$. Because of the nonuniform distribution of active sites as illustrated in Figure 11, the velocity magnitude varies with micro area. According to the momentum conservation, the nonuniformity of gas–solid phase reactions results in a net thrust at particle surface. The pressure distribution on particle surface is illustrated in Figure 14. The net induced thrust is obtained by integrating pressure on the whole particle surface. The magnitude of induced thrust is 0.25 of a single particle gravity in this simulation condition. The thrust induced by chemical reactions is a new force, which is worthy of further study and analysis.

4.3 | Influence of active area

The proportion of active area differs with different coal. In addition, carbon is constantly consumed with the reaction proceeding for a single coal particle. The proportion of active area on particle surface is changing during reaction process. The effect of active area ratio on the induced thrust was studied, based on the simulation conditions in

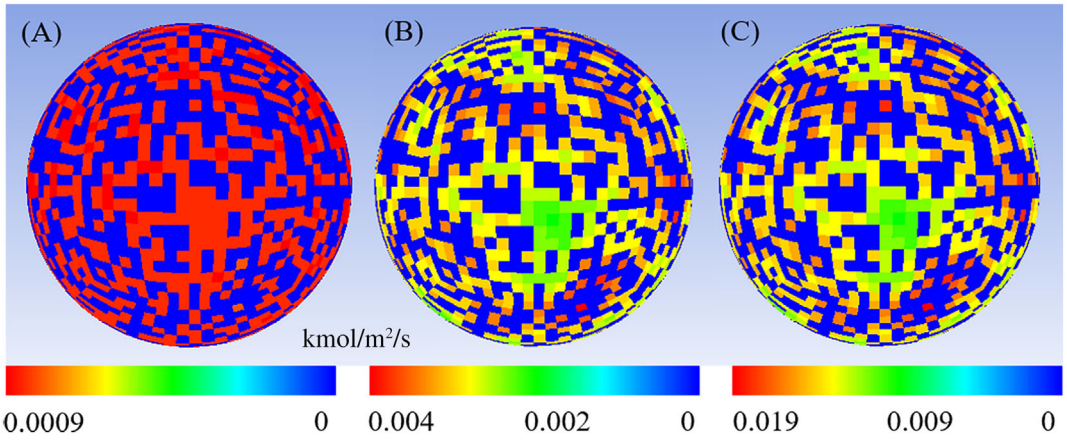

FIGURE 11 Reaction rates on particle surface (A) R4, (B) R5, and (C) R7

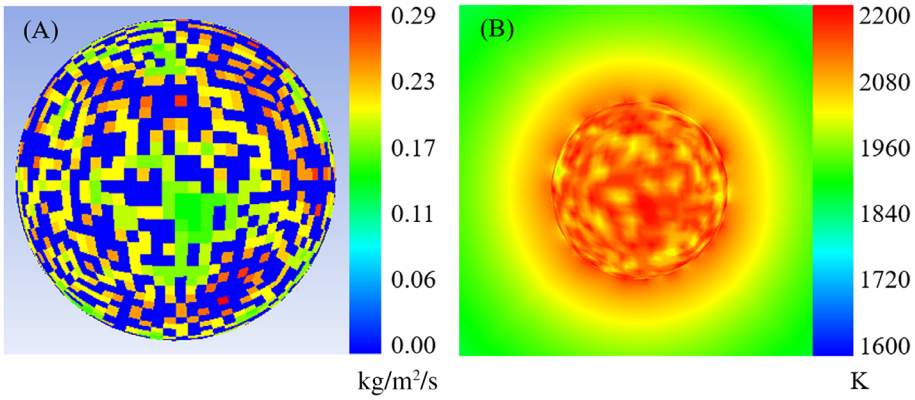

FIGURE 12 (A) Surface consumption rate of carbon and (B) temperature distribution

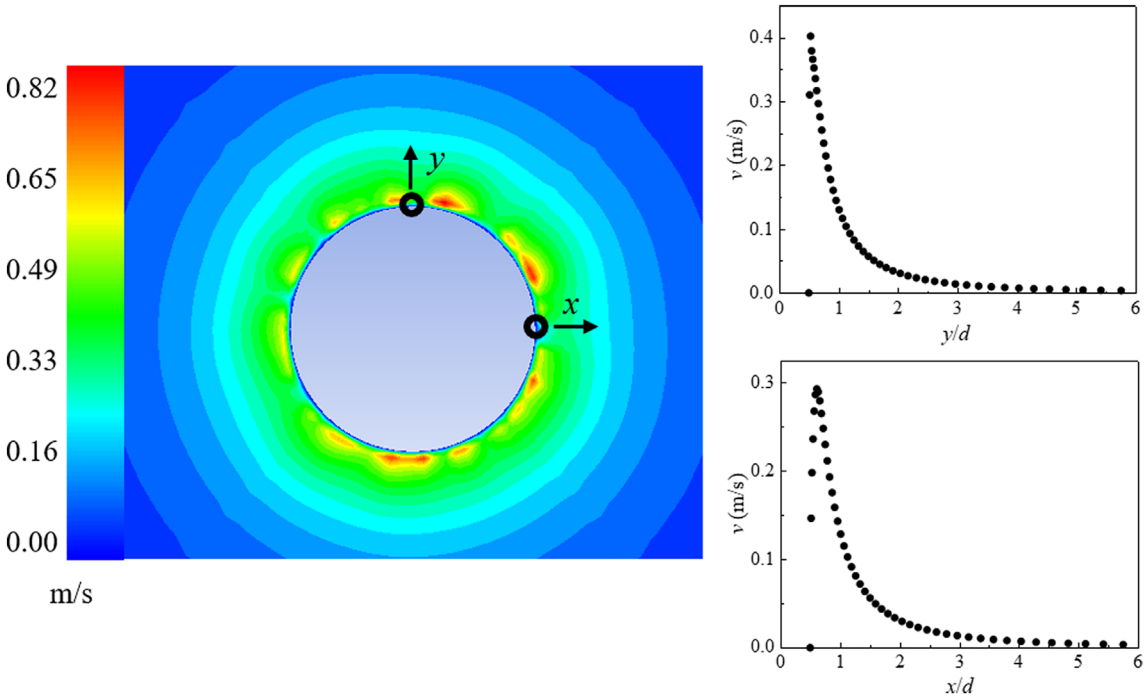

FIGURE 13 Gas velocity magnitude at plane $z = 0$ and velocity distribution in x and y directions

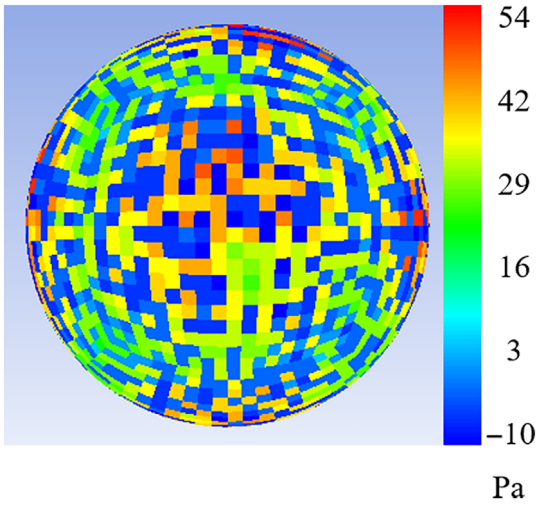

FIGURE 14 Pressure distribution on particle surface

Table 4. Figure 15A shows average induced thrusts of a single particle for different active area ratios (varying between 0.01 and 1). It can be noted that the active area has a great influence on the induced thrust. The $\mathcal{F}$ decreases exponentially with the increase of the active area ratio, when a is between 0.01 and 0.9. When $a = 0.1$, the thrust begins to exceed particle gravity, and it is 1.5 times of particle gravity at $a = 0.01$.

As discussed in Section 2.1, the net thrust is due to the uneven distribution of active sites. According to probability theory, the non-uniformity of active sites distribution on char particle surface varies with different active area ratios. For the local area of particles with

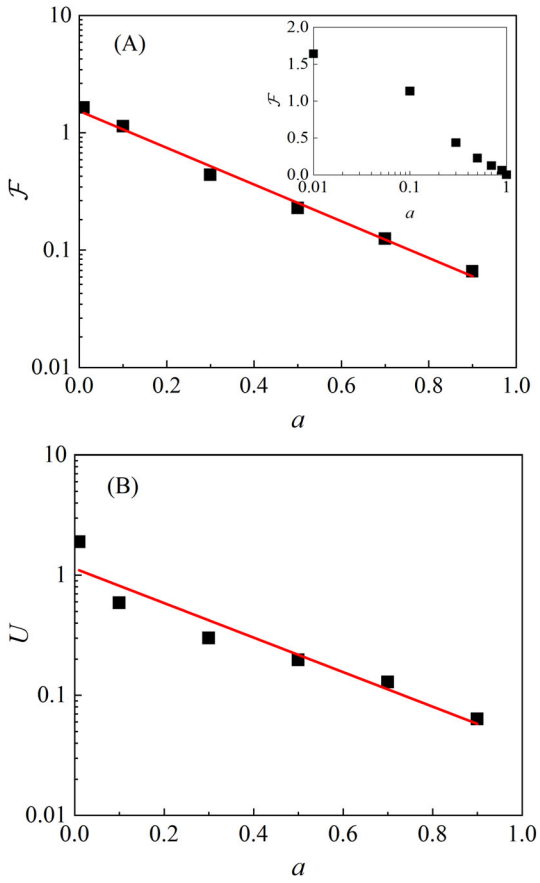

FIGURE 15 (A) The induced thrusts on particles and (B) the nonuniformity ($m = 96$) of active sites distribution for different active area ratios

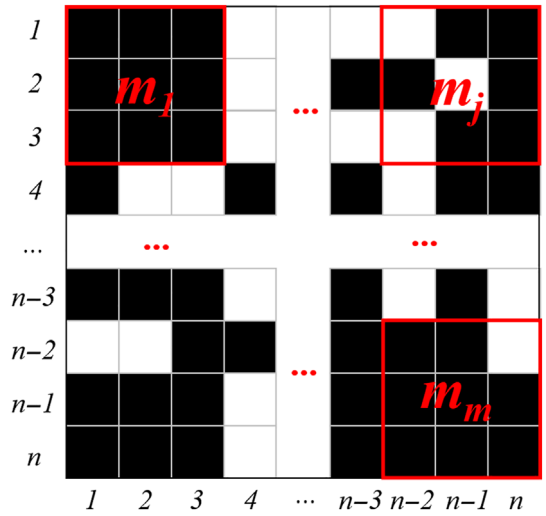

FIGURE 16 Demonstration of the division of sample m_j

cells number $n \times n$, as shown in Figure 16, a nonuniformity index U is introduced to describe the nonuniformity of active sites distribution. Based on nearest neighbor algorithm, the $n \times n$ cells could be evenly divided into m samples. The nonuniformity index U is calculated as follows[48]:

$$U = \sqrt{\frac{\sum_{j=1}^{m} \left(\frac{a_j - a}{a}\right)^2}{m}}, \tag{31}$$

where a_j is the local active cells ratio in sample m_j, and a is the active cells ratio of the whole particle surface. When the active sites are uniformly distributed, U is 0. U increases with the increase of the nonuniformity of active sites distribution. Figure 15B shows the nonuniformity of active sites distribution for different active area ratios. With the increase of the active area ratio, the nonuniformity index U follows exponential decay. The change of induced thrust is basically consistent with the decay trend of the nonuniformity of active sites distribution. In addition, the thrust is also affected by the reaction rate. When $a = 1$, the induced thrust is equal to 0 as shown in Figure 15, because U is 0. The reactions on particle surface are uniform for $a = 1$, forming a force balance.

4.4 | Influence of ambient temperature

Temperature is a crucial factor for chemical reaction. The effect of ambient temperature on the induced thrust was investigated at particle diameter of 150 μm and active area ratio of 0.5. The ambient air temperature was varied in the range of 1473–1873 K. Figure 17 presents the induced thrusts of a single particle and their standard deviations at different ambient temperatures. The $\mathcal{F}$ and its standard deviation increase exponentially with the increase of ambient air temperature. For char combustion, the reaction rate accelerates with the

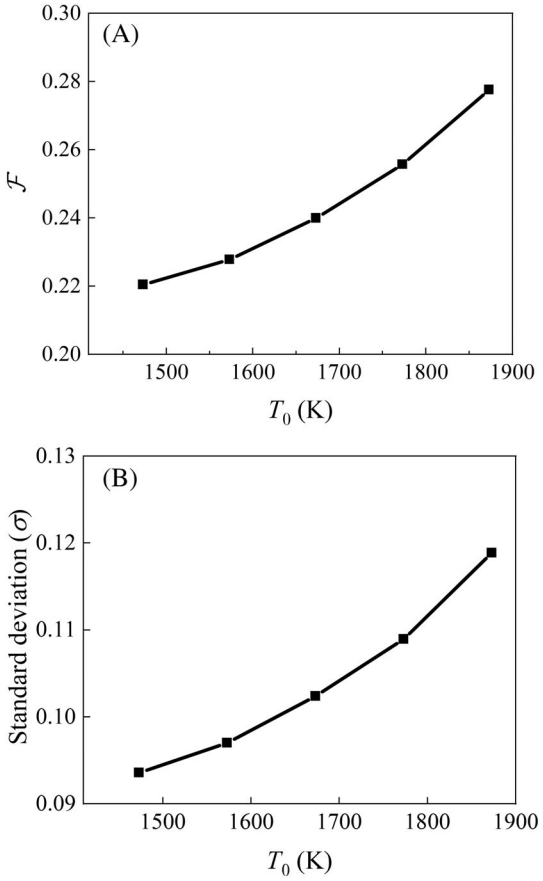

FIGURE 17 (A) The induced thrusts and (B) their standard deviations at different temperature

increase of temperature. Naturally, the release velocity of gaseous products on the particle surface increases. The net force on reacting particle induced by nonuniform gas–solid reactions is enhanced with the increase of ambient air temperature, corresponding with experiments.[11] At $T_0 = 1473$ K, the ratio of induced thrust to single particle weight is about 0.22. At $T_0 = 1873$ K, the $\mathcal{F}$ is about 0.28.

4.5 | Influence of particle diameter

4.5.1 | Induced thrust with different particle diameter

Coal particle size is a vital control condition in entrained flow reactors, which is closely related to particle burnout time and carbon conversion. The qualitative and quantitative effects of particle size on particle-induced thrust are studied at $a = 0.5$, under the working conditions in Table 4. As illustrated in Figure 18, the average surface temperature and the specific carbon consumption rate of particle increase continuously with the decrease of particle size. The specific surface area of particles increases rapidly with the decrease of particle size. The chemical reactions are strengthened[25] for particle with higher specific surface area. The average surface temperature decreases

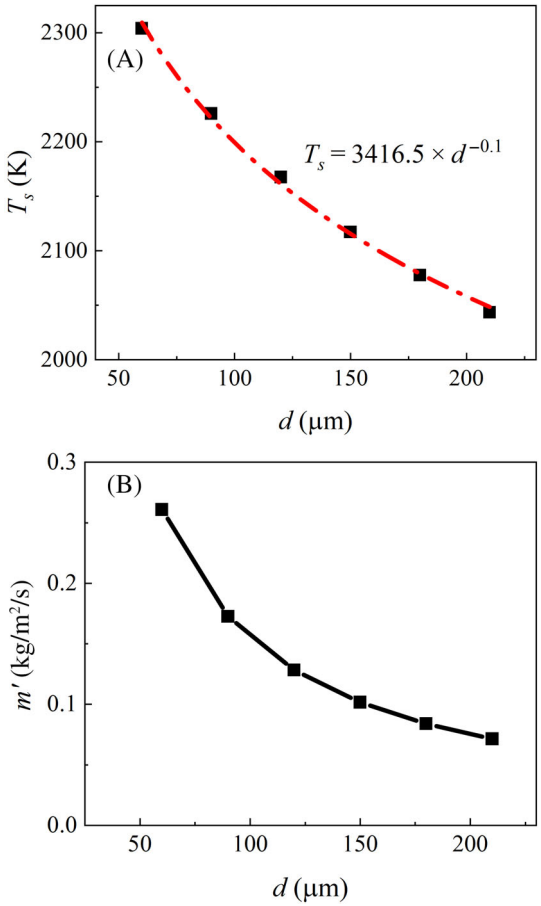

FIGURE 18 (A) The average particle surface temperature T_s and (B) the specific carbon consumption rate m' for different diameters

about 30–60 K, when the particle diameter increases by 30 μm. The particle consumption rates are between 0.07 and 0.26 kg/m^2/s.

Naturally, the induced thrust is enhanced with the decrease of particle diameter, as illustrated in the inset of Figure 19. The gravity force on a single particle decreased with the decrease of the particle size. Therefore, the $\mathcal{F}$ dramatically increased with the particle diameter decreased from 210 to 60 μm, as shown in Figure 19. The $\mathcal{F}$ is about 0.1 at 210 μm. For 100 μm particles, the induced thrust is equivalent to particle gravity. The thrust reaches several times of the particle gravity, when the particle size is reduced to 60 μm. Liu[11] found that the particle motion frequency decreases with the increase of particle size. When the particle size is 250 μm at $T_0 = 1473$ K, no particle fluctuation phenomenon can be observed. For the particle of 250 μm at 1473 K, the numerical result $\mathcal{F}$ should be much smaller than 0.1. This thrust magnitude is too small to overcome the particle friction at sapphire slip in experiments. Our numerical results in this work are in good agreement with the experiments.[11]

4.5.2 | Analysis for the effect of particle diameter

Particle size is the most important parameter affecting particle motion. As mentioned above, the thrust of 60 μm particles is several

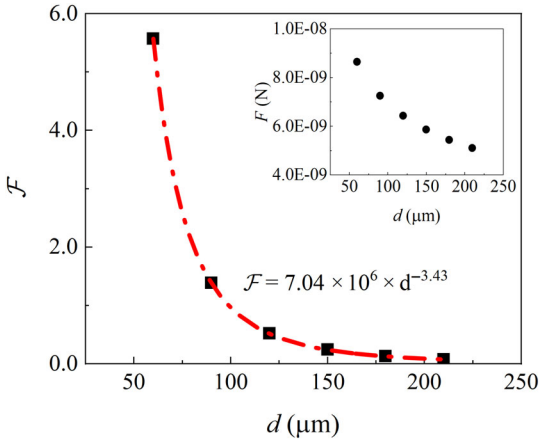

FIGURE 19 The $\mathcal{F}$ for different particle diameter and the fitting curve between them

times of gravity. In order to explain the variation of thrust with particle size, the theoretical analysis is as follows. Figure 18 shows the fitting curve between average surface temperature and particle diameter. Thus, the average surface temperature T_s can be expressed as

$$T_s \propto d^{-0.1}. \tag{32}$$

The global reaction rate R_g on particle surface can be defined as:

$$R_g = k[O_2], \tag{33}$$

where k is rate constant for global reaction. If the effect of O_2 concentration for different particle size is ignored, the relationship between the specific carbon consumption m' and the global reaction rate is as follows:

$$m' \propto R_g \propto k. \tag{34}$$

The rate constant of global reaction at particle surface follows the Arrhenius equation:

$$k = A\exp\left(-\frac{E_a}{RT}\right). \tag{35}$$

Thus:

$$m' = A'\exp\left(-\frac{E_a}{RT}\right). \tag{36}$$

The fitting result between the specific carbon consumption m' and particle surface temperature is shown in Figure 20.

According to Equations (32) and (36) based on the fitted equation shown in Figure 18, the specific carbon consumption is as follows:

$$m' \propto d^{-1.14}. \tag{37}$$

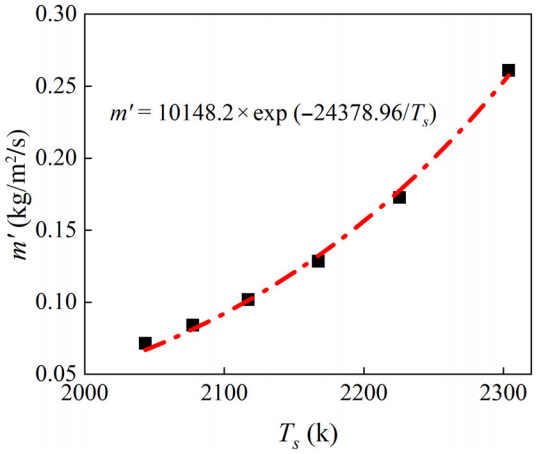

FIGURE 20 The numerical results of specific carbon consumption and particle surface temperature are fitted by the Arrhenius equation

The induced thrust on reacting surface is contributed by the reaction reactants and products fluxes according to the momentum conversion. The contribution of reactants and products to thrust is proportional. According to Equations (1)–(5),

$$F = (m_r \cdot \Delta v_r + m_p \cdot \Delta v_p) \propto m_p \cdot \Delta v_p, \tag{38}$$

where m_r is the rate of gaseous reactants to the particle surface, m_p is the rate of released products. According to the global reaction of carbon consumption, the rate of carbon consumption m_c is proportional to the rate of released products.

$$m_c \propto m_p. \tag{39}$$

The rate of products released from the particle surface can be related to the gas flow rate:

$$m_c = m' \pi d^2 \propto m_p = \pi d^2 \cdot \rho \cdot v_p, \tag{40}$$

$$v_p \propto \frac{m_c}{\pi d^2 \rho} = \frac{m'}{\rho}. \tag{41}$$

The density of gas products follows the ideal gas law:

$$\frac{1}{\rho} = \frac{RT}{PM}. \tag{42}$$

The gas velocity on the particle surface is 0, thus:

$$\Delta v_p = v_p. \tag{43}$$

According to Equation (32) and Equations (37)–(43):

$$F \propto d^{-0.38}. \tag{44}$$

The ratio $\mathcal{F}$ between the induced thrust and the weight of a single particle can be defined as:

$$\mathcal{F} = F/m_s g = \frac{F}{1/6 \pi d^3 \rho_s g}, \tag{45}$$

$$\mathcal{F} \propto d^{-3.38}. \tag{46}$$

The ratio $\mathcal{F}$ is exponential to the particle diameter d. The exponential constant is −3.38 by theoretical derivation and −3.43 by direct fitting for numerical results illustrated in Figure 19. The relative error between theoretical analysis and direct fitting is 1.5%. With the decrease of particle size, the ratio of thrust to particle gravity increases rapidly, so the thrust plays a decisive role in the motion of small particles. The above theoretical analysis qualitatively reveals the mechanism of particle-induced thrust during the combustion process in this article.

5 | CONCLUSION

In this study, the magnitude of induced thrust on reacting char particles was investigated, based on the nonuniform active site distribution during combustion process. The gaseous products are released nonuniformly outward perpendicularly at different active micro areas, directly resulting in the unbalanced induced thrust on a whole particle. The induced thrust of particles with different active areas, ambient gas temperature, and particle size were investigated. The numerical results demonstrated that the thrust magnitude on particles could be equal to that of particle gravity. It is revealed that the induced thrust of a single particle decreases exponentially with the increase of the active area. The net thrust is enhanced with the increase of specific carbon consumption rate. The thrust dramatically increased with the particle diameter decreased from 210 to 60 μm. The ratio between the induced thrust and the particle gravity is exponential to the particle diameter d. This work reveals the mechanism for the net force induced by chemical reactions.

In the present work, coal char is modeled as a spherical particle. When the coal char particles are modeled by nonspherical particles, such as cube, a net torque on particle will be obtained. The nonspherical particles rotate under this net torque. The force induced by nonuniform gas–solid phase reactions affects the motion and rotation of particles. This force can be considered in the modeling of gas–solid reactor, which may make the numerical results more accurate.

ACKNOWLEDGMENTS

This work was supported by the Shanghai Outstanding Technology Leader (Grant number 19XD1434800) and the National Natural Science Foundation of China (Grant numbers 21878082, 21776087).

AUTHOR CONTRIBUTIONS

Shengyu Zhou: Data curation (equal); investigation (equal); writing – original draft (equal). **Zhongjie Shen:** Formal analysis (equal). **Qinfeng**

Liang: Formal analysis (equal). **Jianliang Xu:** Methodology (equal); software (equal); supervision (equal); writing – review and editing (equal). **Zhenghua Dai:** Formal analysis (equal). **Haifeng Liu:** Conceptualization (equal); methodology (equal); supervision (equal).

DATA AVAILABILITY STATEMENT

The data that support the findings of this study are available from the corresponding author upon reasonable request.

ORCID

Jianliang Xu https://orcid.org/0000-0001-9390-6896
Haifeng Liu https://orcid.org/0000-0002-2572-8693

REFERENCES

1. Gong X, Lu W, Guo X, et al. Pilot-scale comparison investigation of different entrained-flow gasification technologies and prediction on industrial-scale gasification performance. *Fuel*. 2014;129:37-44. doi:10.1016/j.fuel.2014.03.030
2. Jana K, Ray A, Majoumerd MM, Assadi M, De S. Polygeneration as a future sustainable energy solution – a comprehensive review. *Appl Energy*. 2017;202:88-111. doi:10.1016/j.apenergy.2017.05.129
3. Higman C, Tam S. Advances in coal gasification, hydrogenation, and gas treating for the production of chemicals and fuels. *Chem Rev*. 2014;114(3):1673-1708. doi:10.1021/cr400202m
4. Sun Y, Zheng S. Influence of particle rotation and partial irradiation on the particle heating up process. *Int Commun Heat Mass*. 2020;119:104892.
5. Kumar M, Ghoniem AF. Multiphysics simulations of entrained flow gasification. Part II: constructing and validating the overall model. *Energy Fuel*. 2011;26(1):464-479.
6. Caixia C, Masayuki H, Toshinori K. Numerical simulation of entrained flow coal gasifers part 1 modeling of coal gasification in an entrained flow gasifer. *Chem Eng Sci*. 2000;55:3861-3874.
7. Watanabe H, Kurose R. Modeling and simulation of coal gasification on an entrained flow coal gasifier. *Adv Powder Technol*. 2020;31(7):2733-2741. doi:10.1016/j.apt.2020.05.002
8. Riaza J, Khatami R, Levendis YA, et al. Single particle ignition and combustion of anthracite, semi-anthracite and bituminous coals in air and simulated oxy-fuel conditions. *Combust Flame*. 2014;161(4):1096-1108. doi:10.1016/j.combustflame.2013.10.004
9. Bai X, Lu G, Bennet T, et al. Combustion behavior profiling of single pulverized coal particles in a drop tube furnace through high-speed imaging and image analysis. *Exp Therm Fluid Sci*. 2017;85:322-330. doi:10.1016/j.expthermflusci.2017.03.018
10. Kang SW, Sarofim AF, Beér JM. Particle rotation in coal combustion statistical experimental and theoretical studies. *Symp (Int) Combust*. 1989;22(1):145-153. doi:10.1016/S0082-0784(89)80020-7
11. Liu M, Shen Z, Liang Q, Liu H. Particle fluctuating motions induced by gas-solid phase reaction. *Chem Eng J*. 2020;388:124348.
12. Zhong S, Baitalow F, Reinmöller M, Meyer B. Relationship between the tensile strength of irregularly shaped coal particles and various fuel properties. *Fuel*. 2019;236:92-99. doi:10.1016/j.fuel.2018.08.140
13. Sadhukhan AK, Gupta P, Saha RK. Characterization of porous structure of coal char from a single devolatilized coal particle: coal combustion in a fluidized bed. *Fuel Process Technol*. 2009;90(5):692-700. doi:10.1016/j.fuproc.2008.12.010
14. Liu M, Bai J, Kong L, Bai Z, He C, Li W. The correlation between coal char structure and reactivity at rapid heating condition in TGA and heating stage microscope. *Fuel*. 2020;260:116318. doi:10.1016/j.fuel.2019.116318
15. Liu Y, Fu P, Zhang B, Yue F, Zhou H, Zheng C. Study on the surface active reactivity of coal char conversion in O_2/CO_2 and O_2/N_2 atmospheres. *Fuel*. 2016;181:1244-1256. doi:10.1016/j.fuel.2016.01.077
16. Watanabe H, Okazaki K. Effect of minerals on surface morphologies and competitive reactions during char gasification in mixtures of O_2 and CO_2. *Proc Combust Inst*. 2015;35(2):2363-2371.
17. He Q, Huang Y, Ding L, Guo Q, Gong Y, Yu G. Effect of partial rapid pyrolysis on bituminous properties: from structure to reactivity. *Energy Fuel*. 2020;34(5):5476-5484. doi:10.1021/acs.energyfuels.9b04439
18. Xu K, Hu S, Su S, et al. Study on char surface active sites and their relationship to gasification reactivity. *Energy Fuel*. 2012;27(1):118-125.
19. Li J, Li Z, Yang Y, Duan Y, Xu J, Gao R. Examination of CO, CO_2 and active sites formation during isothermal pyrolysis of coal at low temperatures. *Energy*. 2019;185:28-38. doi:10.1016/j.energy.2019.07.041
20. Li J, Li Z, Yang Y, Niu J, Meng Q. Room temperature oxidation of active sites in coal under multi-factor conditions and corresponding reaction mechanism. *Fuel*. 2019;256:115901. doi:10.1016/j.fuel.2019.115901
21. Li J, Li Z, Yang Y, Wang C. Study on oxidation and gas release of active sites after low-temperature pyrolysis of coal. *Fuel*. 2018;233:237-246. doi:10.1016/j.fuel.2018.06.039
22. Li J, Li Z, Yang Y, Zhang X. Study on the generation of active sites during low-temperature pyrolysis of coal and its influence on coal spontaneous combustion. *Fuel*. 2019;241:283-296. doi:10.1016/j.fuel.2018.12.034
23. Gil S, Mocek P, Bialik W. Changes in total active centres on particle surfaces during coal pyrolysis, gasification and combustion. *Chem Process Eng*. 2011;32(2):155-169. doi:10.2478/v10176-011-0012-8
24. Roberts MJ, Everson RC, Domazetis G, et al. Density functional theory molecular modelling and experimental particle kinetics for CO_2–char gasification. *Carbon*. 2015;93:295-314. doi:10.1016/j.carbon.2015.05.053
25. Zhang R, Chen Y, Lei K, Liu D. The effects of specific surface area and ash on char gasification mechanisms in the mixture of H_2O, CO_2, H_2 and CO. *Fuel*. 2017;209:109-116. doi:10.1016/j.fuel.2017.07.085
26. Richter A, Nikrityuk PA, Kestel M. Numerical investigation of a chemically reacting carbon particle moving in a hot O_2/CO_2 atmosphere. *Ind Eng Chem Res*. 2013;52(16):5815-5824. doi:10.1021/ie302770j
27. Kestel M, Nikrityuk P, Hennig O, Hasse C. Numerical study of the partial oxidation of a coal particle in steam and dry air atmospheres. *IMA J Appl Math*. 2012;77(1):32-46. doi:10.1093/imamat/hxr071
28. Nikrityuk PA, Gräbner M, Kestel M, Meyer B. Numerical study of the influence of heterogeneous kinetics on the carbon consumption by oxidation of a single coal particle. *Fuel*. 2013;114:88-98. doi:10.1016/j.fuel.2012.10.037
29. Gupta P, Sadhukhan AK, Saha RK. Analysis of the combustion reaction of carbon and lignite char with ignition and extinction phenomena: shrinking sphere model. *Int J Chem Kinet*. 2007;39(6):307-319. doi:10.1002/kin.20245
30. Sadhukhan AK, Gupta P, Saha RK. Analysis of the dynamics of coal char combustion with ignition and extinction phenomena: shrinking core model. *Int J Chem Kinet*. 2008;40(9):569-582. doi:10.1002/kin.20343
31. Sadhukhan AK, Gupta P, Kumar Saha R. Modeling and experimental studies on combustion characteristics of porous coal char: volume reaction model. *Int J Chem Kinet*. 2010;42(5):299-315. doi:10.1002/kin.20483
32. Beckmann AM, Bibrzycki J, Mancini M, Szlęk A, Weber R. Mathematical modeling of reactants' transport and chemistry during oxidation of a millimeter-sized coal-char particle in a hot air stream. *Combust Flame*. 2017;180:2-9. doi:10.1016/j.combustflame.2017.02.026
33. Dierich F, Richter A, Nikrityuk P. A fixed-grid model to track the interface and porosity of a chemically reacting moving char particle. *Chem Eng Sci*. 2018;175:296-305. doi:10.1016/j.ces.2017.09.055

34. Nguyen CB, Scherer J, Hartwich M, Richter A. The morphology evolution of char particles during conversion processes. *Combust Flame*. 2021;226:117-128. doi:10.1016/j.combustflame.2020.11.038
35. Xue Z, Guo Q, Gong Y, Xu J, Yu G. Numerical study of a reacting single coal char particle with different pore structures moving in a hot O_2/CO_2 atmosphere. *Fuel*. 2017;206:381-389. doi:10.1016/j.fuel.2017.06.035
36. Xue Z, Gong Y, Guo Q, Wang Y, Yu G. Conversion characteristics of a single coal char particle with high porosity moving in a hot O_2/CO_2 atmosphere. *Fuel*. 2019;256:115967. doi:10.1016/j.fuel.2019.115967
37. Richter A, Nikrityuk PA, Meyer B. Three-dimensional calculation of a chemically reacting porous particle moving in a hot O_2/CO_2 atmosphere. *Int J Heat Mass Transfer*. 2015;83:244-258. doi:10.1016/j.ijheatmasstransfer.2014.11.090
38. Lee H, Choi S. Motion of single pulverized coal particles in a hot gas flow field. *Combust Flame*. 2016;169:63-71. doi:10.1016/j.combustflame.2016.04.012
39. Turns SR. *An Introduction to Combustion: Concepts and Applications*. McGraw-Hill; 2000.
40. Jones WP, Lindstedt RP. Global reaction schemes for hydrocarbon combustion. *Combust Flame*. 1988;73(3):233-249. doi:10.1016/0010-2180(88)90021-1
41. Libby PA, Blake TR. Burning carbon particles in the presence of water vapor. *Combust Flame*. 1981;41:123-147. doi:10.1016/0010-2180(81)90047-X
42. Caram HS, Amundson NR. Diffusion and reaction in a stagnant boundary layer about a carbon particle. *Ind Eng Chem Fundam*. 1977;16(2):171-181. doi:10.1021/i160062a001
43. Date A. *Introduction to Computational Fluid Dynamics*. Cambridge University Press; 2005.
44. Wang J, Li J, Liu X. *Combustion*. Beijing Institute of Technology Press; 2017. doi:10.13227/j.hjkx.201611110
45. Perry RH. *Perry's Chemical Engineers' Handbook*. 6th ed. McGraw-Hill; 1984.
46. Makino A, Law CK. An analysis of the transient combustion and burnout time of carbon particles. *Proc Combust Inst*. 2009;32(2):2067-2074.
47. Bejarano PA, Levendis YA. Single-coal-particle combustion in O_2/N_2 and O_2/CO_2 environments. *Combust Flame*. 2008;153(1-2):270-287.
48. Yin Y, Tu Z, Zhou J, Shen X, Zang S. An probability density function based investigation on the graphite grain distribution. *Mod Cast Iron*. 2017;37(6):80-84.

How to cite this article: Zhou S, Shen Z, Liang Q, Xu J, Dai Z, Liu H. Numerical simulation analysis of the induced thrust on a char particle in reaction process. *AIChE J*. 2022;68(7):e17702. doi:10.1002/aic.17702